

DOI: 10.1002/ ((please add manuscript number))

**Article type: Full Paper**

**Delaminated CoAl-layered double hydroxide@TiO<sub>2</sub> heterojunction nanocomposites for CO<sub>2</sub> photocatalytic reduction**

Santosh Kumar, Lee J. Durndell, Jinesh C Manayil, Mark A. Isaacs, Christopher M.A. Parlett, Sekar Karthikeyan, Richard E. Douthwaite, Ben Coulson, Karen Wilson and Adam F. Lee\*

Dr. S. Kumar, Dr. L. J. Durndell, Dr. J. C. Manayil, Dr. M. A. Isaacs, Dr. C. M. A. Parlett, Dr. S. Karthikeyan, Prof. K. Wilson, Prof. A.F. Lee

European Bioenergy Research Institute, Aston University, Birmingham B4 7ET, UK  
E-mail: a.f.lee@aston.ac.uk

Dr. R.E. Douthwaite, Mr. B. Coulson  
Department of Chemistry, University of York, York YO10 5DD

Keywords: titania, layered double hydroxides, CO<sub>2</sub>, photocatalysis; nanocomposites

Photocatalytic reduction offers an attractive route for CO<sub>2</sub> utilisation as a chemical feedstock for solar fuels production, but remains challenging due to the poor efficiency, instability and/or toxicity of current catalyst systems. Delaminated CoAl-layered double hydroxide nanosheets (LDH-DS) combined with TiO<sub>2</sub> nanotubes (NTs) or nanoparticles (NPs) are promising nanocomposite photocatalysts for CO<sub>2</sub> reduction. Heterojunction formation between visible light absorbing delaminated CoAl nanosheets and UV light absorbing TiO<sub>2</sub> nanotubes greatly enhances interfacial contact between both high aspect ratio components relative to their bulk counterparts. The resulting synergic interaction confers a significant improvement in photoinduced charge carrier separation, and concomitant aqueous phase CO<sub>2</sub> photocatalytic reduction, in the absence of a sacrificial hole acceptor. CO productivity for a 3

wt% LDH-DS@TiO<sub>2</sub>-NT nanocomposite of 4.57 μmol.g<sub>cat</sub><sup>-1</sup>.h<sup>-1</sup> exhibits a 10- and 5-fold increase over that obtained for individual TiO<sub>2</sub> NT and delaminated CoAl-LDH components respectively, and is double that obtained for 3 wt% bulk-LDH@TiO<sub>2</sub>-NT and 3 wt% LDH-DS@TiO<sub>2</sub>-NP catalysts. Synthesis of delaminated LDH and metal oxide nanocomposites represents a cost-effective strategy for aqueous phase CO<sub>2</sub> reduction.

## 1. Introduction

Artificial photosynthesis as a route to solar fuels from CO<sub>2</sub> and water represents a promising strategy to deliver syngas and hydrocarbons as sustainable feedstocks to support global energy needs and security, and (albeit to a limited extent) mitigate anthropogenic climate change.<sup>[1],[2]</sup> Semiconductor nanostructures are promising inorganic mimics of biological photocatalysts in this regard, offering diverse and tunable photophysical and electronic properties.<sup>[3],[4],[5]</sup> Titania is the best known and most widely studied inorganic photocatalyst due to its abundance and low cost, photostability, established redox chemistry, UV absorption, and low toxicity.<sup>[6]</sup> However, due to the wide band gap of pure titania, and extensive recombination of photoexcited charge carriers, various strategies have been exploited to improve its photophysical properties including doping<sup>[7]</sup> and heterojunction formation,<sup>[8]</sup> which offer enhanced hydrogen generation<sup>[9]</sup> and CO<sub>2</sub> reduction.<sup>[10]</sup> The development of photocatalytic systems with suitable redox behaviour to drive solar fuels production remains challenging,<sup>[11],[12]</sup> with the majority of research involving titania systems requiring either a redox mediator<sup>[13]</sup> or an sacrificial electron/hole scavengers<sup>[14]</sup> and hence lowering the atom efficiency. Scalable solar fuels production requires low cost and stable materials able to catalyze both photochemical redox reactions without additional reagents.<sup>[15]</sup> Photocatalytic

CO<sub>2</sub> reduction is also problematic due to its poor solubility in aqueous systems, and the weak affinity of many inorganic semiconductors.<sup>[16]</sup>

A range of low dimensional, layered, porous and/or hybrid inorganic nanomaterials have been investigated for photocatalytic CO<sub>2</sub> reduction, with the primary goal being improved charge carrier separation and transport characteristics and/or morphology, and hence apparent quantum yields and activity<sup>[3],[4],[10]</sup> Layered double hydroxides (LDHs) have emerged as promising photocatalysts for CO<sub>2</sub> photoreduction due to their tunable band gap (spanning the UV to visible region), high CO<sub>2</sub> adsorption capacity, relative ease of scale-up, nanoporous architecture, fabrication from earth abundant elements, and conduction and valence energies amenable for driving both CO<sub>2</sub> reduction and water oxidation.<sup>[17],[18],[19]</sup> The first application of a zinc-copper- Al or Ga (III)-LDH<sup>[18]</sup> for CO<sub>2</sub> photocatalytic reduction found CO and methanol, and various LDHs have been subsequently explored spanning divalent metal cations such as Mg, Co, Ni, Zn, and trivalent cations such as Al, In, Ga and Cr within their interlayers.<sup>[19]</sup> NiIn-LDHs are the most promising to date for aqueous phase CO<sub>2</sub> photocatalytic reduction to CO, with a productivity of 3.6 µmol.g<sup>-1</sup>.h<sup>-1</sup> under UV light,<sup>[17]</sup> while defective ZnAl-LDHs are effective for vapor phase CO<sub>2</sub> reduction to CO under UV irradiation.<sup>[20]</sup> However, pristine LDHs generally exhibit poor quantum efficiency under solar irradiation due to slow charge carrier mobility and high rates of electron-hole recombination.<sup>[19]</sup> Strategies to improve LDH performance include the use of noble metal (Pt, Pd and Au)<sup>[21]</sup> co-catalysts as electron acceptors, or their combination with wide band gap semiconductors<sup>[22]</sup> to improve utilization of the solar spectrum and/or charge separation. Titania is a good acceptor of photoexcited electrons,<sup>[23]</sup> and the valence band maximum (VBM)<sup>[24]</sup> potential of certain LDH materials<sup>[25]</sup> lie above that of titania (and are hence able to accept photoexcited

holes from the latter) yet at an energy sufficient to overcome the overpotential for water oxidation (0.653 eV<sup>[26]</sup>). We therefore recently synthesized a nanocomposite photocatalyst for aqueous CO<sub>2</sub> photocatalytic reduction, comprising commercial P25 titania in contact with a CoAl-layered double hydroxide (LDH). This exhibited promising activity (2.2 μmol.g<sup>-1</sup>.h<sup>-1</sup>) and >80 % selectivity to CO, without requiring a sacrificial hole scavenger.<sup>[27]</sup> The superior performance of this type-II heterojunction photocatalyst was attributed to increased photoexcited charge carrier lifetimes relative to its individual UV and visible light absorbing semiconductor components, attributed to the spatial separation of charge carriers due to electron transfer from CoAl-LDH→P25, and concomitant hole transfer from P25→CoAl-LDH, and extended utilization of the solar spectrum. Optimizing the heterojunction interface between titania and LDH components should afford a facile means to further improve photocatalytic performance following rational design principles (such as maximizing the interfacial contact area).

Here, the preceding design strategy is extended through the synthesis of new heterojunction nanocomposites comprising delaminated CoAl-LDH nanosheets dispersed within matrices of high aspect TiO<sub>2</sub> nanoparticles or nanotubes. These nanocomposites enable decoupling of the relative importance of the dimensions/morphology of the visible light (hole-driven) CoAl-LDH<sup>[27],[28]</sup> and UV light (electron-driven) TiO<sub>2</sub> semiconductors<sup>[8],[27]</sup> on CO<sub>2</sub> photocatalytic reduction. CoAl-LDH thickness and titania morphology both strongly influence aqueous CO<sub>2</sub> reduction, with the combination of delaminated CoAl-LDH nanosheets with TiO<sub>2</sub> nanotubes delivering 4.57 (2.0) μmol.g<sub>cat</sub><sup>-1</sup>.h<sup>-1</sup> of CO and 0.41 (0.1) μmol.g<sub>cat</sub><sup>-1</sup>.h<sup>-1</sup> of CH<sub>4</sub> under UV-Vis (visible) irradiation, through a stoichiometric redox process and in the absence of sacrificial agents.

## 2. Results and Discussion

### 2.1. Structural properties of CoAl-LDH and TiO<sub>2</sub> components

The synthesis of parent CoAl-LDH and TiO<sub>2</sub> nanostructures is summarized in **Scheme S1**.

Powder XRD of the parent CoAl-LDH and CoAl-LDH-DS materials shown in **Figure S1a** confirmed that both exhibited (d<sub>00n</sub>) reflections characteristic of the desired layered double hydroxide (JCPDF#51-0045). However, the intensity of the (d<sub>00n</sub>) reflections was significantly suppressed in the delaminated material indicating a loss of long range order and delamination along the (d<sub>00n</sub>) planes, while the (d<sub>012</sub>) peak intensity remained similar to the parent LDH indicating that intralayer crystallinity was retained. The interlayer spacing of the parent CoAl-LDH was 0.84 nm (determined from the d<sub>003</sub> reflection), consistent with the presence of interlayer NO<sub>3</sub><sup>2-</sup> anions and water.<sup>[29]</sup> ICP-OES confirmed that the Co:Al stoichiometry was approximately 2:1 ratio for both parent and delaminated materials (**Table S1**). Note that delamination of CoAl-LDH containing interlayer nitrate anions upon hydrothermal treatment has been previously reported,<sup>[29]</sup> in contrast to the behaviour observed for more stable CoAl-LDH containing interlayer carbonate anions. This stability difference is ascribed to the lower crystallinity of LDH materials prepared with interlayer nitrate versus carbonate anions, which makes assist in deconstructing the former. Our previous study on nanocomposites containing bulk CoAl-LDHs in conjunction with P25 indicated that the Co:Al ratio had negligible impact on CO<sub>2</sub> photoreduction performance (**Figure S2**), and hence the Co:Al stoichiometry was not investigated in this work.

TEM of the parent CoAl-LDH revealed the sand rose structure characteristic of layered double hydroxides, comprising agglomerates of nanoplatelets approximately 40 nm thick (**Figure 1a-b**) and several hundred nanometers across. Successful delamination was directly

visualized by TEM, with **Figure S1c-d** and **Figure 1c-f** evidencing low contrast (as anticipated given their ultrathin nature) sheets in the CoAl-LDH-DS material, with a morphology and diameter similar to those of the parent but whose thickness was decreased from 40 nm to only 2-4 nm (**Figure S1c-d** and **Figure 1c-d**); the latter dimension is consistent with LDH nanosheets only 1-4 layers thick as indicated in **Figure 1d**. Lattice fringes of CoAl-LDH-DS observed in **Figure 1f** confirmed the delaminated nanosheets were crystalline, with a ( $d_{012}$ ) spacing of 0.272 nm identical to that of the parent CoAl-LDH.<sup>[28]</sup> Light scattering upon irradiation of the CoAl-LDH-DS solution by a red laser (the Tyndall effect<sup>[30]</sup>) evidenced the highly dispersed colloidal nature of the nanosheets, which was stable for >6 months (in contrast the suspended parent CoAl-LDH precipitated within minutes). N<sub>2</sub> porosimetry of both LDH materials (**Figure S1b**) showed type II adsorption-desorption isotherms characteristic of macroporous materials (or non-porous materials possessing large interparticle voids) with H3-type hysteresis loops attributed to non-rigid aggregates of plate-like particles under IUPAC classifications.<sup>[31]</sup> The BET surface area of CoAl-LDH-DS was 67 m<sup>2</sup>.g<sup>-1</sup>, twice that of the parent CoAl-LDH (36 m<sup>2</sup>.g<sup>-1</sup>).

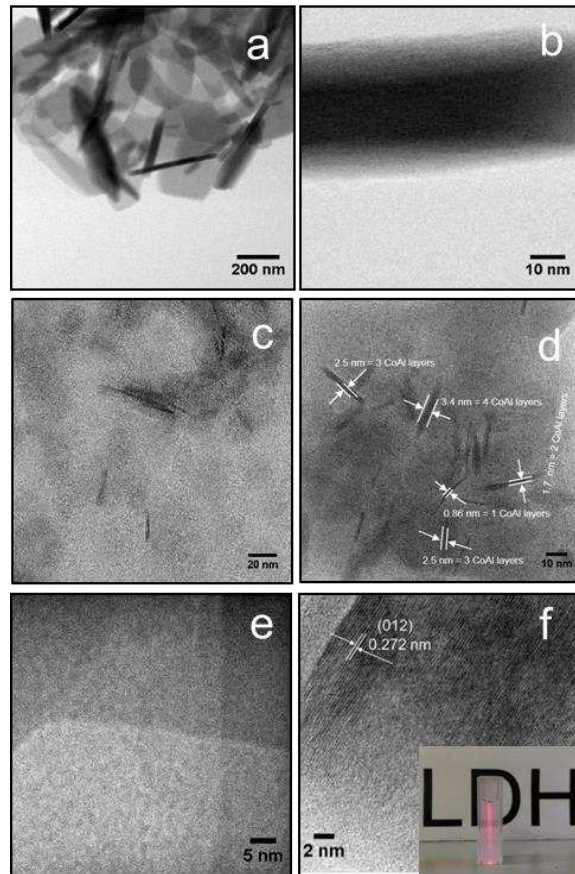


**Figure 1.** Low and high resolution TEM images of (a-b) CoAl-LDH and (c-f) CoAl-LDH-DS. Inset photographs show the light scattering behaviour of suspended CoAl-LDH particles.

The morphologies of TiO<sub>2</sub>-NT and TiO<sub>2</sub>-NP materials were also investigated by XRD and TEM. **Figure S3a** revealed both nanostructured titanias were pure anatase, unlike P25 which is a 4:1 mixture of rutile and anatase phases. **Figure 2** and **Figure S4** show that the TiO<sub>2</sub>-NT comprised uniform, high aspect ratio hollow tubes, with diameters between 6-8 nm and extending for few hundred nanometres in length. The tube wall thickness was <2 nm (**Figure S4e-f**), while the (d<sub>001</sub>) and (d<sub>101</sub>) planar spacings of 0.24 nm and 0.35 nm respectively confirmed the nanotubes were anatase titania.<sup>[32],[33]</sup> TiO<sub>2</sub>-NP comprised uniform, approximately 5 nm diameter spherical anatase particles. These nanostructures were tightly packed in both cases, with the resulting interparticle voids expected to confer micro- or

mesoporosity, as reflected in their type IV adsorption-desorption isotherms (**Figure S3b**),<sup>[31]</sup> and high surface areas ( $229\text{-}250 \text{ m}^2\cdot\text{g}^{-1}$ ) relative to non-porous TiO<sub>2</sub>- P25 ( $54 \text{ m}^2\cdot\text{g}^{-1}$ ).

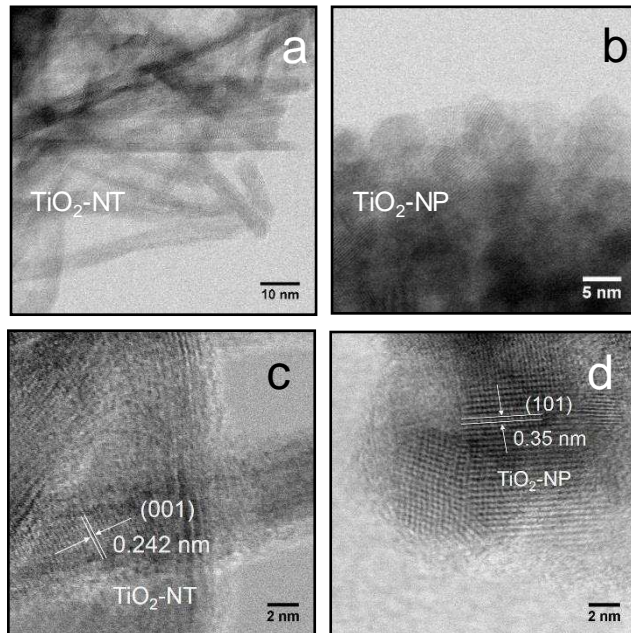
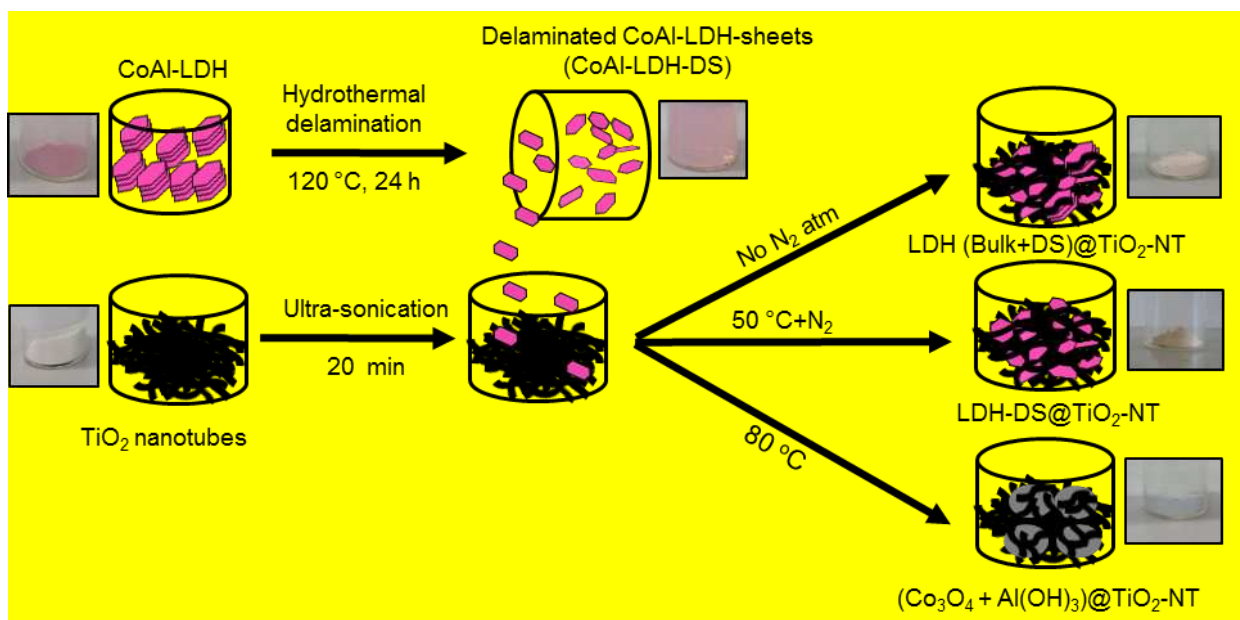


**Figure 2.** Low and high resolution TEM images of (a,c) TiO<sub>2</sub>-NT, and (b,d) TiO<sub>2</sub>-NT.

## 2.2 CoAl-LDH@TiO<sub>2</sub> nanocomposites

Synthesis of Co-LDH-DS@TiO<sub>2</sub> nanocomposites is summarized in **Scheme 1**.

Nanocomposites containing around 3 wt% of the LDH component prepared without a protective N<sub>2</sub> atmosphere suffered partial reconstruction of the delaminated CoAl-LDH-DS, evidenced by a very weak, but characteristic (d<sub>003</sub>) reflection at 11 ° by powder XRD (**Figure S5**), possibly due to the presence of CO<sub>3</sub><sup>2-</sup> ions from dissolved atmospheric CO<sub>2</sub> attracting LDH sheets together,<sup>[29]</sup> while those prepared >80 °C resulted in LDH decomposition and concomitant Al(OH)<sub>3</sub> and Co<sub>3</sub>O<sub>4</sub> (and/or (Co(OH)<sub>2</sub>) formation.<sup>[34],[35]</sup> Optimal synthetic conditions were therefore determined as 50 °C under a N<sub>2</sub> atmosphere. A common Co:Al stoichiometry of 2:1 was maintained for all nanocomposites in this work (**Table S1**).



**Scheme 1.** Schematic of CoAl-LDH@TiO<sub>2</sub> nanocomposite synthesis.

High resolution TEM images of 3 wt % LDH-DS@TiO<sub>2</sub>-NT and 3 wt % LDH-DS@TiO<sub>2</sub>-NP

NP (**Figure 3a-b** and **Figure S6**) evidence intimate contact between the titania nanostructures and delaminated CoAl-LDH nanosheets, with lattice fringes for each component identical to those observed prior to their mixing. EDX elemental mapping confirmed a uniform distribution of CoAl-LDH throughout the titania nanotubes and nanoparticles matrices (**Figure S7** and **Figure S8** respectively).

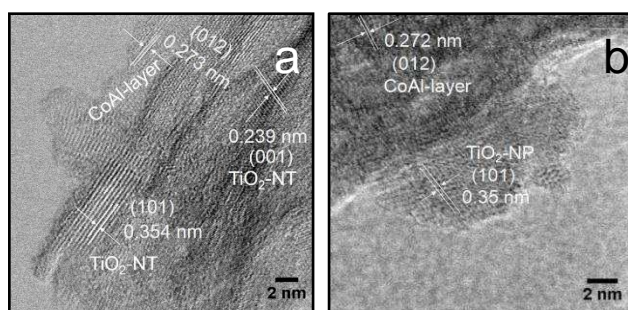


**Figure 3.** High resolution TEM images (a) 3 wt% LDH-DS@TiO<sub>2</sub>-NT, and (b) LDH-DS@TiO<sub>2</sub>-NP nanocomposites.

XRD patterns of the preceding nanocomposites exhibited only anatase reflections (**Figure S9**, the low CoAl-LDH-DS concentration prohibiting observation of associated reflections) consistent with HRTEM, while a 3 wt % LDH-DS@TiO<sub>2</sub>-P25 reference material prepared identically also exhibited anatase and rutile reflections from the parent commercial titania. Volume averaged particles sizes of titania crystallites were unchanged from their parent values (Table S1). Together with HRTEM, these findings confirm the retention of ordered LDH and titania phases within the nanocomposites. Nitrogen porosimetry of the 3 wt% CoAl-LDH-DS@TiO<sub>2</sub> nanocomposites showed adsorption-desorption isotherms dominated by the parent titania characteristics, with 3-5 nm mesopores evident for the nanotube and nanoparticle materials (**Figure S10a-b**), as anticipated from the low loading of LDH incorporated. A slight reduction in surface area (and pore volume and BJH pore diameter) on introducing CoAl-LDH-DS into the nanotube and nanoparticle matrices was observed (**Table S1** and **Figure S10b**), consistent with that expected for a physical mixture of the two components. HRTEM, XRD and porosimetry together evidence the successful integration of CoAl-LDH nanosheets only a few layers thick, and delaminated along the (d<sub>00n</sub>) planes within TiO<sub>2</sub> nanostructures.

### 2.3. Photophysical properties of CoAl-LDH@TiO<sub>2</sub> nanocomposites

The electronic structure and optical properties of 3 wt% CoAl-LDH-DS@TiO<sub>2</sub> nanocomposites, and constituent titania and LDH components, were subsequently investigated by XPS, UV-Vis and time-resolved photoluminescence spectroscopies. **Figure 3a** shows Ti 2p XP spectra for the parent titania nanotubes and nanoparticles, alongside their corresponding nanocomposites. In all cases, a single spin-orbit split doublet was observed with 2p<sub>3/2</sub> and 2p<sub>1/2</sub> peaks centered around 458.1 and 463.7 eV respectively, consistent with

Ti<sup>4+</sup> species in TiO<sub>2</sub>.<sup>[28]</sup> The Co 2p XP spectrum of CoAl-LDH-DS also exhibited a single spin-orbit split doublet (**Figure 3b**) and hence chemical environment, with 2p<sub>1/2</sub> and 2p<sub>3/2</sub> peaks centered around 796.7 and 780.8 eV and satellites at 801.3 and 786.5 eV indicative of high-spin divalent Co<sup>2+</sup> species within the CoAl-LDH layers.<sup>[36]</sup> A small increase in the Co 2p<sub>3/2</sub> binding energy (to 781.3 eV), and concomitant decrease in the Ti 2p<sub>3/2</sub> binding energy (to 457.8 eV), was observed for the 3 wt % CoAl-LDH-DS@TiO<sub>2</sub>-NT relative to the individual components. This may reflect an initial state effect arising from electron transfer from the CoAl-LDH-DS to TiO<sub>2</sub>-NT component, and provides tentative evidence for direct electronic contact (heterojunction formation) between the semiconductors.

DRUV spectra of 3 wt% CoAl-LDH-DS@TiO<sub>2</sub> nanocomposites, and constituent titania and LDH components are shown in **Figure 3c**. All titania materials exhibited strong UV absorption, with a sharp cut-off ~380 nm for nanotubes, and ~390 nm for anatase nanoparticles and P25, translating to optical band gaps of 3.21 (TiO<sub>2</sub>-NT), and 3.14 eV (TiO<sub>2</sub>-NP) (**Figure S11a-b**).<sup>[37]</sup> The slight band gap widening for the TiO<sub>2</sub>-NT may arise from quantum confinement effects<sup>[38]</sup> within the thin (< 2nm) walls, which are expected as the semiconductor dimensions fall below twice the exciton Bohr radius (estimated between 1-3.2 nm for anatase<sup>[39],[40]</sup>). The DRUV spectrum of CoAl-LDH exhibited two distinct absorption bands, a broad band in the visible region centered around 558 nm, and a sharper UV band around 300 nm; delamination shifted the middle band to ~520 nm, and resulted in the appearance of additional absorption band around 670 nm. The bands 520-558 nm are indicative of the 4T1g(F) → 4T1g(P) transition of Co<sup>2+</sup> octahedrally coordinated by weak-field ligands,<sup>[27],[41]</sup> while that at 670 nm band corresponds to a 3A2g(F)→3T1g(F) transition arising from spin-orbit coupling.<sup>[41],[42]</sup> The UV absorption may arise from ligand→metal

charge transfer within the CoAl-LDH layer. These absorption features translate to optical band gaps of 2.12 and 2.18 eV for CoAl-LDH and CoAl-LDH-DS respectively (**Figure S11c-d**), consistent with literature reports.<sup>[28],[43]</sup> The 3 wt% CoAl-LDH@TiO<sub>2</sub> nanocomposites exhibited spectra intermediate between those of their constituent components, albeit dominated by the majority titania component, featuring strong UV absorption arising from TiO<sub>2</sub> nanotubes/nanoparticles and a weak visible light response from the delaminated CoAl-LDH nanosheets. Heterojunction formation between semiconductor components is indicated by a shift in the nanocomposite UV absorption cut-offs to higher wavelength relative to the pure TiO<sub>2</sub> nanostructures, particularly noticeable for the 3 wt% CoAl-LDH@TiO<sub>2</sub>-NT material.

Valence band maximum (VBM) edge potentials of titania and CoAl-LDH-DS components were also determined by valence band XPS<sup>[27]</sup> (**Figure S12**) from the intercept of the tangent to the density of states at the Fermi edge as 2.69 eV (TiO<sub>2</sub>-NP), 2.75 eV (TiO<sub>2</sub>-NT) and 1.25 eV (CoAl-LDH-DS). These VBM were used in conjunction with the preceding optical band gap energies to calculate corresponding conduction band minimum (CBM) potentials of -0.45 eV (TiO<sub>2</sub>-NP), -0.46 eV (TiO<sub>2</sub>-NT) and -0.93 eV (CoAl-LDH-DS).<sup>[25]</sup> These energy levels and associated band offsets are shown in **Figure S13**, and indicative of a type-II (staggered) band alignment at the CoAl-LDH-DS@TiO<sub>2</sub> interface, with  $\Delta E_{\text{VBM}} = 0.42 \text{ eV}$  and 1.29 eV and  $\Delta E_{\text{CBM}} = 0.26 \text{ eV}$  and 0.27 eV for the 3 wt % CoAl-LDH-DS@TiO<sub>2</sub>-NT and 3 wt % CoAl-LDH-DS@TiO<sub>2</sub>-NP respectively. Heterojunction formation is accompanied by band bending between the CoAl-LDH-DS and TiO<sub>2</sub> components. This band alignment is considered advantageous for the separation of photogenerated holes and electrons,<sup>[44]</sup> favoring hole accumulation on the CoAl-LDH-DS nanosheets (and consequent water oxidation) and

electron accumulation on the titania nanostructures (and consequent CO<sub>2</sub> reduction), and hence both halves of the full redox reaction without additional (molecular) charge acceptors.

Photoinduced charge carrier recombination within the 3 wt% CoAl-LDH-DS@TiO<sub>2</sub> nanocomposites, and Co-Al-LDH-DS and TiO<sub>2</sub> reference materials, was probed through steady state<sup>[45]</sup> and time-resolved<sup>[46]</sup> PL spectroscopy. All TiO<sub>2</sub> nanostructures exhibited two characteristic emissions under irradiation with 320 nm light (**Figure S14**); one around 400 nm arising from an interband transition,<sup>[47]</sup> and a second weaker emission around 470 nm attributed to the recombination of charges localised on oxygen vacancies.<sup>[47]</sup> CoAl-LDH and CoAl-LDH-DS also exhibited two emissions at 400 nm and 470 nm, attributed to ligand field splitting and corresponding 4A<sub>2</sub>g→4T<sub>1</sub>g (F) and 4T<sub>2</sub>g→4T<sub>1</sub>g (F) transitions often reported for octahedral cobalt(II) compounds.<sup>[46],[41]</sup> The emissions in CoAl-LDH-DS were significantly reduced relative to the parent CoAl-LDH, indicating suppressed charge recombination. Despite the high titania loading in all three 3 wt% CoAl-LDH-DS@TiO<sub>2</sub> nanocomposites, their corresponding emissions were significantly reduced relative to the parent TiO<sub>2</sub> component, indicating suppressed charge recombination (improved charge separation), presumably due to the migration of photoexcited electrons from the CB of CoAl-LDH-DS to that of the TiO<sub>2</sub> matrix, and concomitant photoexcited hole migration from the VB of the TiO<sub>2</sub> matrix to the VB of CoAl-LDH-DS. Emission from the 3 wt% CoAl-LDH-DS@TiO<sub>2</sub>-NT was especially weak compared to its nanoparticle and P25 analogues, possibly due to more extensive heterojunction formation observed by XPS and greater valence band bending ( $\Delta E_{VB/M}$  decreasing from 1.5 → 0.42 for the nanotube composite versus 1.44 → 1.29 for the nanoparticle analogue).

Time-resolved PL measurements provided additional confirmation for reduced charge carrier recombination within the 3 wt% LDH-DS@TiO<sub>2</sub> nanocomposites (**Figure 3d**).<sup>[46]</sup> Average charge carrier lifetimes ( $\tau$ ) were determined from fitting the resulting decay curves with a biexponential function (**Table S2**), which reflect non-radiative and radiative relaxation processes originating from the direct formation of free charge carriers and the indirect formation of self-trapped excitons. In all cases, the nanocomposites displayed longer  $\tau$  values (i.e. slower recombination) than their CoAl-LDH-DS and TiO<sub>2</sub> constituents, with the 3 wt% CoAl-LDH-DS@TiO<sub>2</sub>-NT exhibiting the slowest electron-hole pair recombination of  $\tau = 6.7$  ns versus 5.5 ns (TiO<sub>2</sub>-NT) and 4.8 ns (CoAl-LDH-DS). This modified electronic transport provides further evidence for heterojunction formation (and an excellent synergy) between the delaminated CoAl-LDH nanosheets and the TiO<sub>2</sub> matrices they are dispersed within.

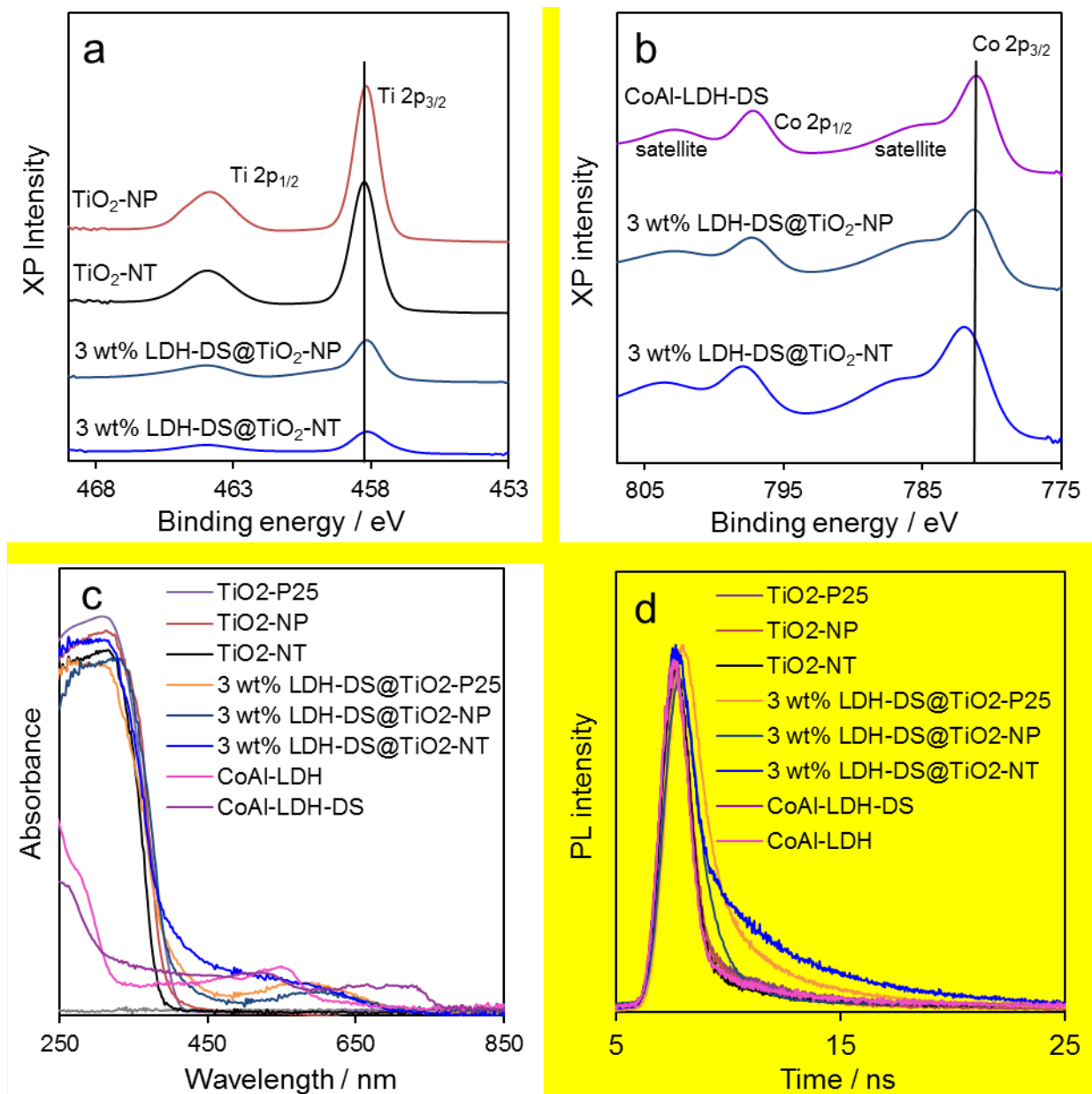


**Figure 3.** (a) Ti 2p and (b) Co 2p XP spectra, (c) DRUVS, and (d) time-resolved PL spectra at 380 nm excitation wavelength of 3 wt% LDH-DS@TiO<sub>2</sub> nanocomposites alongside CoAl-LDH and TiO<sub>2</sub> references.

## 2.4. Photocatalytic CO<sub>2</sub> reduction over CoAl-LDH@TiO<sub>2</sub> nanocomposites

The photocatalytic performance of CoAl-LDH@TiO<sub>2</sub> nanocomposites was subsequently investigated for aqueous phase CO<sub>2</sub> reduction under UV-Vis irradiation by a 300 W Xe lamp in the absence of a sacrificial hole acceptor. Control experiments were first performed in the absence of either CO<sub>2</sub>, water, catalyst or light (**Figure S15**) to confirm that CO<sub>2</sub> and water

were the only sources of carbon and hydrogen in photocatalytic products.<sup>[27],[48]</sup> Only gaseous products of photocatalysis were observed, namely CO<sub>2</sub>, H<sub>2</sub>, O<sub>2</sub> and (exceptionally) methane.

Individual TiO<sub>2</sub> nanostructures (P25, TiO<sub>2</sub>-NP, and TiO<sub>2</sub>-NT) exhibited very low activity for either CO<sub>2</sub> reduction or water oxidation (**Figure 4** and **Table S3**), presumably due to a combination of their small CBM potentials (~0.45 eV) which is insufficient to drive effectively CO<sub>2</sub>+2H+2e<sup>-</sup>→CO+H<sub>2</sub>O (E<sup>0</sup> = -0.53 eV at pH 7), fast photoexcited charge carrier recombination and low CO<sub>2</sub> absorptivity (Table S1). However, this CBM potential is sufficient to drive proton reduction to hydrogen (-0.41 eV at pH 7), and indeed H<sub>2</sub> was evolved over all titanias, albeit at a low rate due to rapid charge recombination commonly observed in the absence of either a noble metal co-catalyst to trap photo-excited electrons, and/or organic scavengers to trap photoexcited holes.<sup>[14]</sup> Among the titanias, TiO<sub>2</sub>-NTs exhibited the highest photocatalytic activity, which we attribute to its high aspect ratio, thin walls, comparatively slow charge recombination ( $\tau$  = 5.5 ns versus 4.8 and 1.5 ns for TiO<sub>2</sub>-NP and P25 respectively) and short diffusion length for photoexcited charges to reach the nanotube surface. The parent Co-Al-LDH and delaminated CoAl-LDH-DS nanosheets both exhibited slightly improved CO production relative to titanias (as expected for their higher CBM potential of ~0.93 eV), with delamination conferring a 20 % enhancement (1.06 versus 0.83 μmol.h<sup>-1</sup>.g<sup>-1</sup>) as a result of the associated increase in surface area and CO<sub>2</sub> adsorption capacity seen in **Table S1**, and concomitant decrease in charge recombination shown in **Figure 3d** and **Table S2**. However, neither performance was especially impressive, likely an inability to drive both sides of the redox reaction in the absence of a charge carrier acceptor. In contrast, all CoAl-LDH@TiO<sub>2</sub> nanocomposites showed superior CO productivity to, and hence a strong synergy between, the LDH and titania components. The 3 wt% CoAl-LDH-

DS@TiO<sub>2</sub>-NT nanocomposite exhibited the highest CO productivity of 4.57 μmol.g<sup>-1</sup>.h<sup>-1</sup>, almost 7.5 and 5 times that of its TiO<sub>2</sub>-NT and CoAl-LDH-DS constituents respectively (and twice that of 20 wt% P25@CoAl-LDH)<sup>[27]</sup>, in addition to 0.41 μmol.g<sup>-1</sup>.h<sup>-1</sup> CH<sub>4</sub>; this equates to a CO+CH<sub>4</sub> selectivity >94 % (**Table S3**). This synergy must arise from a convolution of increased spectral utilization (UV and visible), charge carrier separation/ lifetime, and CO<sub>2</sub> affinity for the heterojunction nanocomposite. All components and nanocomposites displayed (CO or H<sub>2</sub>):O<sub>2</sub> product stoichiometries close to 2:1, as expected since CO<sub>2</sub> reduction to CO and H<sub>2</sub>O reduction to H<sub>2</sub> are both 2e<sup>-</sup> processes, whereas water oxidation is a 4e<sup>-</sup> process (2H<sub>2</sub>O → O<sub>2</sub> + 4H<sup>+</sup> + 4e<sup>-</sup>). For 3 wt% CoAl-LDH-DS@TiO<sub>2</sub>-NT, a CH<sub>4</sub>:O<sub>2</sub> stoichiometry of 1:2 was also observed, consistent with the 8e<sup>-</sup> reduction to form methane from CO<sub>2</sub>. It is noteworthy that methane was only produced over the 3 wt% LDH-DS@TiO<sub>2</sub>-NT photocatalyst, which exhibits the longest charge carrier lifetimes (**Table S2**), consistent with the slower kinetics expected for this more demanding multi-electron reduction.

CO productivity over the 3 wt% CoAl-LDH-DS@TiO<sub>2</sub>-NT photocatalyst was more than double that achieved for the 3 wt% CoAl-LDH@TiO<sub>2</sub>-NT or 3 wt% LDH-DS@TiO<sub>2</sub>-NP materials. The physicochemical properties including phase, crystallite size, surface area and CO<sub>2</sub> chemisorption capacity of these three photocatalysts are almost identical (**Table S1**), as are the optical band gaps of their CoAl-LDH/CoAl-LDH-DS and TiO<sub>2</sub>-NT/TiO<sub>2</sub>-NP components. Hence, this rate enhancement can only be ascribed to more efficient heterojunction formation between visible light absorbing delaminated CoAl-LDH-DS nanosheets and UV light absorbing high aspect ratio TiO<sub>2</sub> nanotubes in the 3 wt% CoAl-LDH-DS@TiO<sub>2</sub>-NT.

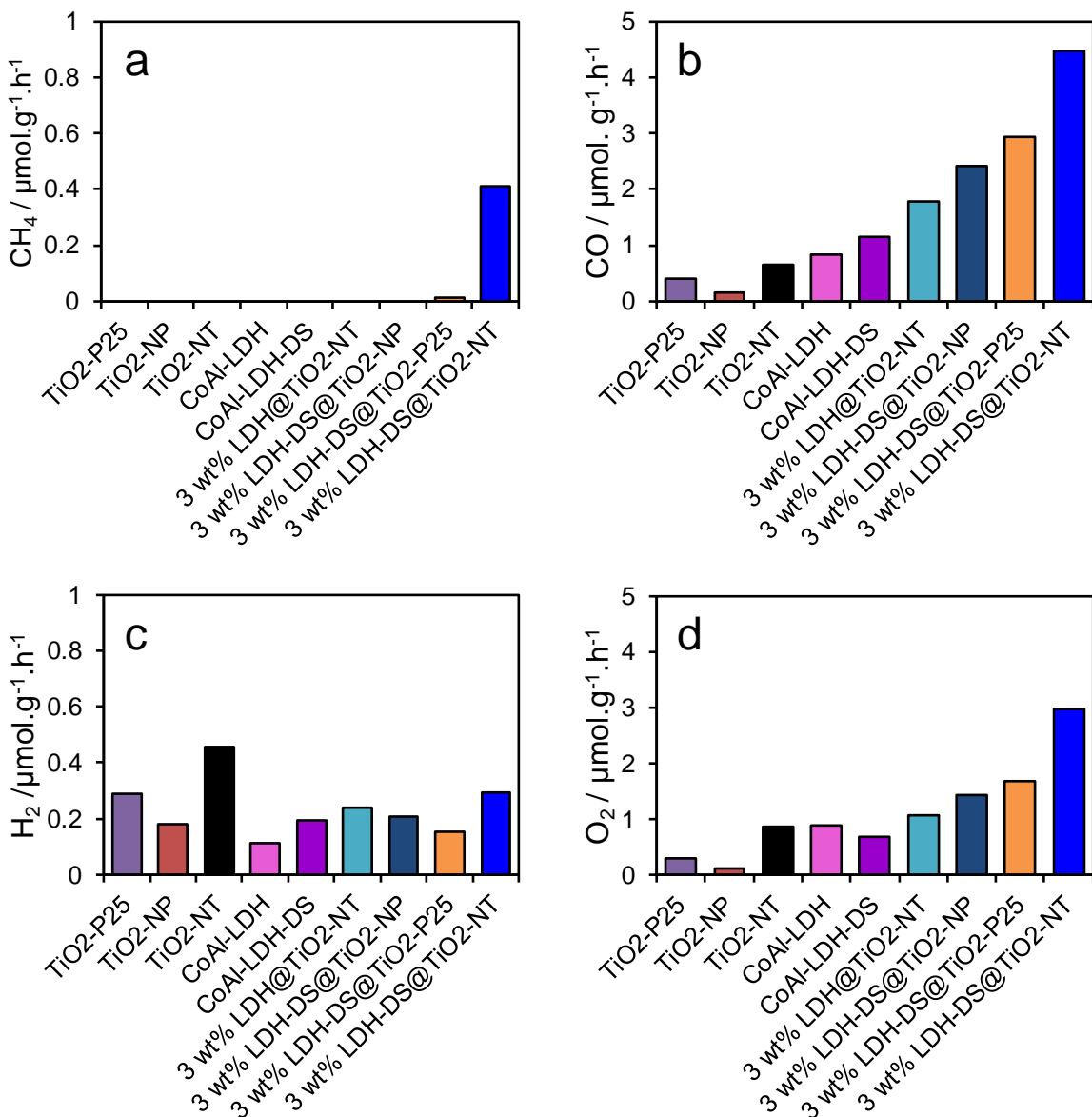


**Figure 4.** (a)  $\text{CH}_4$ , (b)  $\text{CO}$ , (c)  $\text{H}_2$  and (d)  $\text{O}_2$  mass-normalized productivity averaged over the first 4 h of aqueous phase  $\text{CO}_2$  photoreduction over 3 wt% LDH-DS@ $\text{TiO}_2$  nanocomposites, and CoAl-LDH and  $\text{TiO}_2$  references under UV-Vis irradiation by a 300 W Xe lamp.

The impact of heterojunction formation and role of the titania component in the nanocomposites was further examined by comparing UV-Vis versus visible light (employing a 400 nm cut-off filter) photocatalytic  $\text{CO}_2$  reduction over the 3 wt% LDH-DS@ $\text{TiO}_2$ -NT and constituent  $\text{TiO}_2$  nanotube and CoAl-LDH-DS. Under visible light irradiation, the nanotubes were catalytically inactive, as expected for the wide band gap semiconductor, whereas the

CoAl-LDH-DS evolved small quantities of CO and O<sub>2</sub> (**Figure 5**). However, the lower CO and CH<sub>4</sub> reduction productivities of the nanocomposite compared to those observed under UV-Vis irradiation (2.0 versus 4.5  $\mu\text{mol.h}^{-1}.\text{g}^{-1}$  CO, and 0.1 versus 0.4  $\mu\text{mol.h}^{-1}.\text{g}^{-1}$  CH<sub>4</sub>) suggest that significant electron-hole recombination occurs within the delaminated CoAl-LDH-DS nanosheets in the absence of simultaneous titania photoexcitation, i.e. two-step photon excitation of both semiconductors is superior to LDH excitation alone. Under UV-Vis irradiation, titania can act as both a hole-donor, promoting water oxidation over the LDH, and as an electron-acceptor. This observation highlights the importance of charge separation across the heterojunction interface of 3 wt% LDH-DS@TiO<sub>2</sub>-NT nanocomposite in enhancing the poor intrinsic visible light photooxidation activity of the delaminated CoAl-LDH-DS, and poor intrinsic UV photoreduction activity of TiO<sub>2</sub>-NT. Apparent quantum efficiencies (AQE) for CO production over 3 wt% LDH-DS@TiO<sub>2</sub>-NT are around 0.26 % and 0.09 % under 365 nm (using a UV band pass filter) and 475 nm (visible band pass filter) irradiation (**Table S4**), respectively. These AQEs are much higher than corresponding values of <0.1 % (UV) for P25@CoAl-LDH<sup>[27]</sup> or reduced graphene oxide-amine-titanium dioxide nanocomposites<sup>[49]</sup> or ZrOCo<sup>II</sup>-IrO<sub>x</sub> SBA-15<sup>[50]</sup> wafer or Pt-TiO<sub>2</sub><sup>[51]</sup> heterogeneous photocatalysts. They are also much greater than many ‘high performance’ photocatalysts such as TiO<sub>2</sub> nanofibres (0.036%)<sup>[52]</sup> and SrNb<sub>2</sub>O<sub>6</sub> plates (0.065%)<sup>[51]</sup> under UV irradiation, and Co<sub>3</sub>O<sub>4</sub> hexagonal platelets under visible light<sup>[53]</sup> (0.069%, wherein a visible light sensitizer [Ru(bpy)<sub>3</sub>]Cl<sub>2</sub> and hole scavenger TEOA were also required). The combined quantum efficiency for CO+CH<sub>4</sub> is also higher than those reported Ag/Ag<sub>2</sub>SO<sub>3</sub> (0.12 %)<sup>[54]</sup> and Ag/AgIO<sub>3</sub> (0.19%)<sup>[55]</sup>, photocatalysts for CO<sub>2</sub> reduction to CO+CH<sub>4</sub>, featuring noble metal electron traps and water vapour as the proton donor (albeit CH<sub>4</sub> was the major product).

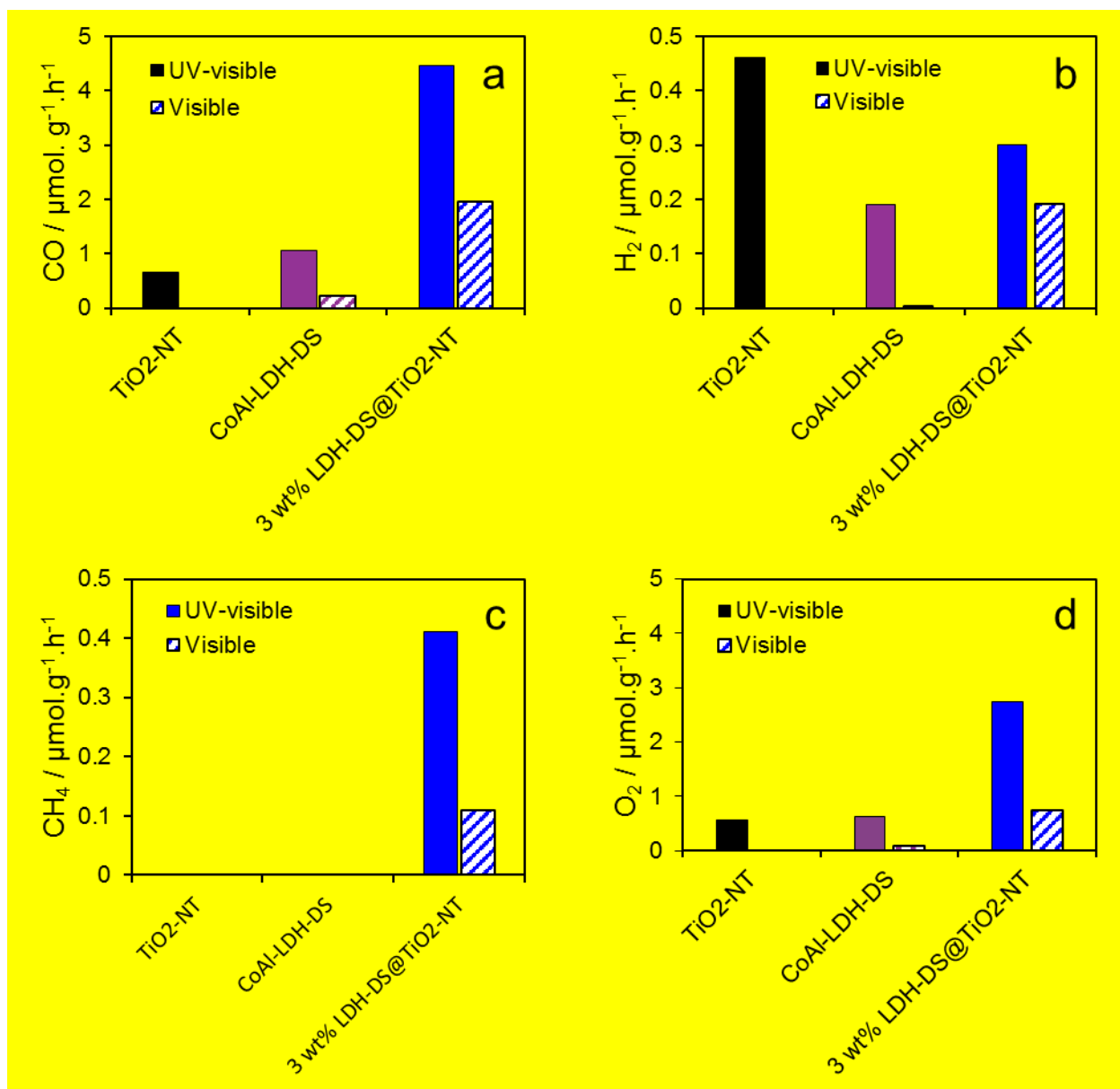
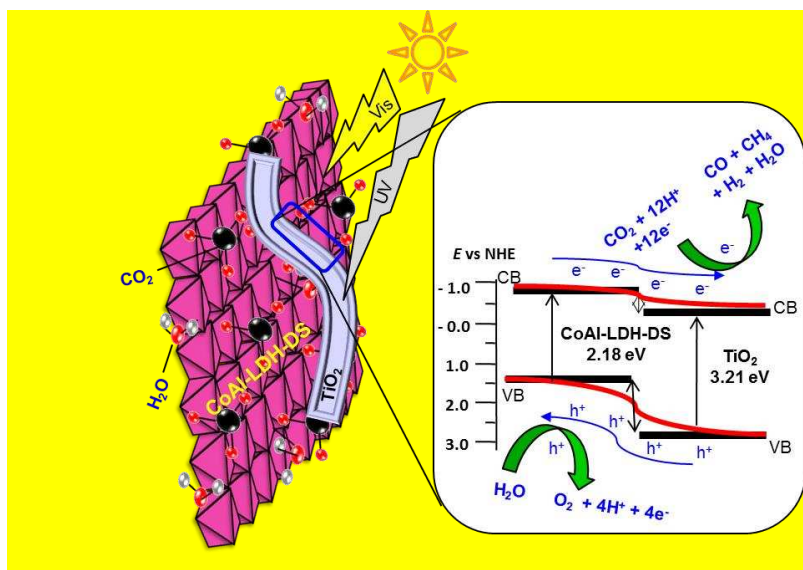


**Figure 5.** Comparison of (a) CH<sub>4</sub>, (b) CO, (c) H<sub>2</sub> and (d) O<sub>2</sub> mass-normalized productivity averaged over the first 4 h of aqueous phase CO<sub>2</sub> photoreduction over 3 wt% LDH-DS@TiO<sub>2</sub>-NT nanocomposite, and CoAl-LDH-DS and TiO<sub>2</sub>-NT references under UV-Vis versus visible only light irradiation.

Photocatalytic CO<sub>2</sub> reduction over 3 wt% CoAl-LDH-DS@TiO<sub>2</sub>-NT is proposed to occur in a similar fashion to that previously advanced.<sup>[27]</sup> Briefly, under visible light irradiation, due to the type-II band alignment between the LDH and titania, electrons photoexcited into the LDH conduction band migrate via the heterojunction into the titania conduction band, where they reduce CO<sub>2</sub> (adsorbed at the LDH surface) into CO and CH<sub>4</sub> as illustrated in **Scheme 2**. Under

UV irradiation, photoexcited holes simultaneously migrate from valence band of titania via the heterojunction into the LDH valence band, where they may be trapped at  $\text{Co}^{2+}$  sites to produce  $\text{Co}^{3+}$  or  $\text{Co}^{4+}$  which in turn oxidize  $\text{H}_2\text{O}$  to liberate  $\text{O}_2$ , regenerate  $\text{Co}^{2+}$ , and release protons which migrate to the interface with titania where they combine with electrons and/or molecular carbon species to form  $\text{H}_2$ ,  $\text{CO}$  or  $\text{CH}_4$ .<sup>[56],[57]</sup> The combination of delaminated CoAl-LDH-DS nanosheets and high aspect ratio anatase  $\text{TiO}_2$  nanotubes creates a large heterojunction interface across which photoinduced charge carrier separation, and the preceding redox chemistry, can occur. Such charge separation extends charge carrier lifetimes sufficient to facilitate the challenging multi-electron reduction of  $\text{CO}_2$  to  $\text{CH}_4$ . Delaminated CoAl-LDH-DS nanosheets promote aqueous phase catalytic  $\text{CO}_2$  photoreduction by harnessing visible light, adsorbing  $\text{CO}_2$  from solution, and promoting water oxidation. Future studies will explore routes to induce ordering between the LDH and anatase components, for example through surfactant templating approaches and/or spatial localization within hierarchically porous scaffolds,<sup>59</sup> and to further improve the heterojunction interface through either reducing the dimensions of the delaminated CoAl-LDH nanosheets, or shortening the anatase nanotubes to enhance interpenetration between the semiconductor components.



**Scheme 2.** Proposed mechanism of  $\text{CO}_2$  photocatalytic reduction over CoAl-LDH-DS@ $\text{TiO}_2$ -NT heterojunction nanocomposite.

### 3. Conclusion

A facile wet-chemical route has been developed to prepare CoAl-LDH-DS@TiO<sub>2</sub> nanocomposites via the dispersion of (visible light absorbing) delaminated CoAl-layered double hydroxide nanosheets within matrices of (UV absorbing) anatase nanotubes (NT) or nanoparticles (NP). The resulting CoAl-LDH-DS@TiO<sub>2</sub> nanocomposites show significant rate enhancements and improved apparent quantum efficiency for the aqueous phase catalytic CO<sub>2</sub> photoreduction to CO and CH<sub>4</sub>, in the absence of sacrificial agents. Maximum CO productivity was obtained for 3 wt% CoAl-LDH@TiO<sub>2</sub>-NT, being 5-7.5 times higher than that of its constituent TiO<sub>2</sub> or delaminated CoAl-LDH nanosheet components, and >twice as active as nanocomposites containing either bulk CoAl-LDH or anatase NPs. Superior photocatalytic reduction of the CoAl-LDH-DS@TiO<sub>2</sub> nanocomposites reflects formation of a staggered type-II heterojunction across the interface between these high aspect ratio semiconductors, which permits efficient photoexcited charge separation resulting from electron transfer from the CoAl-LDH-DS to titania, and concomitant reverse hole transfer from titania into the CoAl-LDH TiO<sub>2</sub> nanostructure. Selectivity to (CO+CH<sub>4</sub>) reached >90 % relative to H<sub>2</sub> evolution under full spectrum irradiation. This synthetic strategy could be readily extended to prepare diverse mixed oxide/hydroxide nanocomposites for applications including water splitting, waste water depollution, fuel cells and energy storage.

### Experimental Section

Materials: Reagents Co(NO<sub>3</sub>)<sub>2</sub>·6H<sub>2</sub>O (Sigma, 99 %), Al(NO<sub>3</sub>)<sub>3</sub>·9H<sub>2</sub>O (Sigma, 99 %), P25 (Sigma), and hexamine (Sigma, 99.9%), titanium (IV) n-butoxide (ACROS Organics, 99.0 %), sulfuric acid (Fisher, 98%), hydrochloric acid (Fisher, 37 %), ethanol (Fisher, analytical reagent grade), sodium hydroxide (ACROS Organics, 99 %) were used as received. All other

chemical reagents used in this work were analytical grade and used without further purification.

TiO<sub>2</sub> nanostructures synthesis: TiO<sub>2</sub> nanoparticles and nanotubes were synthesized following solvothermal and hydrothermal literature methods (**Scheme S1a**).<sup>[58]</sup> For anatase TiO<sub>2</sub> nanoparticles (TiO<sub>2</sub>-NP), 5.1 g titanium (IV) n-butoxide was added dropwise to 70 mL absolute ethanol under vigorous stirring at room temperature, followed by 0.33 mL sulfuric acid and 0.3 mL deionized water. The resulting solution was transferred to a 100 ml Teflon autoclave and aged for 4 h at 180 °C under air to yield a white solid, which was then washed thoroughly with ethanol and dried at 60 °C for 5 h. For anatase TiO<sub>2</sub> nanotubes (TiO<sub>2</sub>-NT), 0.5 g of the preceding TiO<sub>2</sub>-NP was added to a 50 mL 10 M NaOH aqueous solution in a Teflon autoclave at room temperature, and aged for 24 h at 150 °C for 24 h. The resulting solid was dispersed in 500 ml 0.1 M HCl aqueous solution for 12 h under constant stirring at room temperature, then centrifuged (5000 rpm and 5 min) and washed thoroughly with deionized water and subsequently ethanol, dried at 60 °C for 5 h, and finally calcined at 400 °C for 2 h under flowing O<sub>2</sub> (20 ml/min).

LDH nanostructure synthesis: CoAl-LDH (**Scheme S1b**) and delaminated CoAl-LDH nanosheets were prepared following a (carbonate-free) hydrothermal literature method.<sup>[29]</sup> For the parent CoAl-LDH, 0.06 mols Co(NO<sub>3</sub>)<sub>2</sub>·6H<sub>2</sub>O, 0.03 mols Al(NO<sub>3</sub>)<sub>3</sub>·9H<sub>2</sub>O, and 0.012 mols hexamethylenetetramine were dissolved in 200 mL deionised and degassed water. The resulting solution was purged with N<sub>2</sub> at room temperature under constant stirring, and then aged in a 500 mL round bottom flask at 80 °C for 48 h under N<sub>2</sub> without stirring. The precipitate (cake) obtained was washed with deionized water until the washing were of neutral

pH, and subsequently dried overnight at 60 °C in vacuo to yield the final CoAl-LDH which was stored in a vacuum desiccator. Delaminated CoAl-LDH nanosheets (LDH-DS) were prepared by adding 2.5 g of the preceding pH neutral CoAl-LDH cake to 50 mL deionised and degassed water in a Teflon autoclave, prior to ageing at 120 °C for 12 h. Residual parent CoAl-LDH was removed by centrifugation at 2000 rpm for 30 min, leaving a colloidal solution of the CoAl-LDH-DS material (2.4 g. L<sup>-1</sup>) which was purged with N<sub>2</sub> at 50 °C, sealed with parafilm and stored in a desiccator. A powder reference sample of delaminated CoAl-LDH nanosheets was also prepared by evaporation of the colloidal solution under N<sub>2</sub>.

CoAl- LDH@TiO<sub>2</sub> nanocomposites synthesis: CoAl-LDH@TiO<sub>2</sub> nanocomposites were prepared by ultrasonic dispersion followed by deposition-evaporation. Briefly, 200 mg of synthesized TiO<sub>2</sub>-NT, TiO<sub>2</sub>-NP, or commercial TiO<sub>2</sub>-P25, was dispersed in deionized and degassed water by ultrasonication (Elmasonic S100H, 5 min, 550 W/50 Hz), to which a desired mass of parent CoAl-LDH, or volume of CoAl-LDH-DS colloidal solution, was added. The resulting suspension was stirred at room temperature under N<sub>2</sub> for 24 h, and water subsequently evaporated at 50 °C to yield the nanocomposite. The mass of CoAl-LDH-DS was also varied from 1 to 5 wt% to produce a family of CoAl-LDH-DS@TiO<sub>2</sub>-NT composites. Note that composites containing 3 wt% CoAl-LDH-DS were the most active for the photocatalytic reduction of CO<sub>2</sub> (**Figure S16**), and hence were selected for detailed study in this work.

Catalyst characterization: Powder X-ray diffraction (XRD) patterns were recorded on a Bruker-AXS D8 ADVANCE diffractometer operated at 40 kV and 40 mA using Cu K<sub>α</sub> radiation (0.15418 nm) between 10-80° in 0.02° steps. X-ray photoelectron spectroscopy was

performed on a Kratos Axis HSi spectrometer with a monochromated Al K<sub>α</sub> X-ray source operated at 90 W and magnetic charge neutralizer. Spectral processing was performed using CasaXPS version 2.3.16, with energy referencing to adventitious carbon at 284.6 eV, and surface compositions and peak fitting derived using appropriate instrumental response factors and common line shapes for each element. Nanostructure morphology was visualized on a JEOL JEM-2100 HAADF-STEM operating at 200 kV accelerating voltage, with elemental mapping performed by energy-dispersive X-ray spectroscopy (EDX) using an Oxford INCA EDX detector. Porosimetry was performed through N<sub>2</sub> physisorption at 77 K using a Quantachrome Nova 4000e porosimeter. Brunauer–Emmett–Teller (BET) surface areas were calculated over the relative pressure range 0.01–0.2. Pore size distributions were calculated by applying the BJH method to desorption isotherms for relative pressures >0.35. CO<sub>2</sub> chemisorption was performed on samples degassed at 120 °C using a He carrier gas on a Quantachrome ChemBET PULSAR TPR/TPD/TPO instrument. Diffuse reflectance UV-Vis spectra (DRUVS) were measured on a Thermo Scientific Evo220 spectrometer using an integrating sphere and KBr as standard and samples diluted in KBr. Optical band gaps were calculated from Tauc plots as described in the supporting information. Steady state photoluminescence (PL) spectra of samples were recorded on a F-4500FL spectrometer at an excitation wavelength of 320 nm. PL lifetime data were collected on an Edinburgh Photonics FLS 980 spectrometer using a picosecond pulsed LED light with an excitation wavelength of 380 nm.

Photocatalytic CO<sub>2</sub> reduction: Photocatalytic CO<sub>2</sub> reduction was carried out at room temperature in a sealed 320 ml stainless steel photoreactor with a quartz window and a 300 W Xe light source. 50 mg of sample was dispersed in 5 ml of water by ultrasonication for 5 min

and charged in the photoreactor. Prior to irradiation, the reaction mixture was degassed in the dark with CO<sub>2</sub> at 1 bar for 2 h to saturate the solution with CO<sub>2</sub>, and then continuously irradiated with UV-Vis light using a 300 W Xe Toption Group. Ltd TOP-X300 lamp (spectral output shown in our previous report<sup>[27]</sup>). Aliquots of the reaction mixture were periodically withdrawn using a 1 ml gas syringe for analysis on a Shimadzu Tracera GC-2010 Plus chromatograph fitted with a Carboxen1010 (30mx 0.53mmx0.1μm) column and Barrier Ionization Detector. Liquid products were also analysed periodically from separate aliquots on an Agilent 1260 HPLC fitted with a Hi Plex column; no carbon-containing liquid products were detected in this study. P25 was calcined in air at 200 °C for 4 h prior to use in control experiments to remove any trace carbonaceous residues; without calcination, small quantities of CO and CH<sub>4</sub> were evolved during control experiments under nitrogen in the absence of CO<sub>2</sub>. Selectivity towards reactively-formed H<sub>2</sub>, CO and CH<sub>4</sub> was calculated from **Equation 1**, **2** and **3** below:<sup>[27]</sup>

$$\text{H}_2 \text{ selectivity / \%} = \frac{2N_{\text{H}_2}}{8N_{\text{CH}_4} + 2N_{\text{CO}} + 2N_{\text{H}_2}} \times 100 \quad (1)$$

$$\text{CO selectivity / \%} = \frac{2N_{\text{CO}}}{8N_{\text{CH}_4} + 2N_{\text{CO}} + 2N_{\text{H}_2}} \times 100 \quad (2)$$

$$\text{CH}_4 \text{ selectivity / \%} = \frac{2N_{\text{CH}_4}}{8N_{\text{CH}_4} + 2N_{\text{CO}} + 2N_{\text{H}_2}} \times 100 \quad (3)$$

where N<sub>CH<sub>4</sub></sub>, N<sub>CO</sub> and N<sub>H<sub>2</sub></sub> are the yields of reactively-formed CH<sub>4</sub>, CO and H<sub>2</sub> respectively.

Apparent quantum yields were calculated as described in the supporting information at either 365 (UV) or 475 (Visible) nm.

**Supporting Information**

Supporting Information is available from the Wiley Online Library or from the author.

**Acknowledgements**

We thank the EPSRC (EP/K021796/1 and EP/K029525/2) for financial support.

Received: ((will be filled in by the editorial staff))

Revised: ((will be filled in by the editorial staff))

Published online: ((will be filled in by the editorial staff))

- [1] T. Faunce, S. Styring, M. R. Wasielewski, G. W. Brudvig, A. W. Rutherford, J. Messinger, A. F. Lee, C. L. Hill, H. deGroot, M. Fontecave, D. R. MacFarlane, B. Hankamer, D. G. Nocera, D. M. Tiede, H. Dau, W. Hillier, L. Wang, R. Amal, Energy & Environmental Science **2013**, 6, 1074.
- [2] P. V. Kamat, The Journal of Physical Chemistry C **2007**, 111, 2834.
- [3] W. Tu, Y. Zhou, Z. Zou, Advanced Materials **2014**, 26, 4607.
- [4] D. Chen, X. Zhang, A. F. Lee, Journal of Materials Chemistry A **2015**, 3, 14487.
- [5] L. Zhang, Z.-J. Zhao, J. Gong, Angewandte Chemie International Edition, doi:10.1002/anie.201612214.
- [6] K. Nakata, A. Fujishima, Journal of Photochemistry and Photobiology C: Photochemistry Reviews **2012**, 13, 169.
- [7] J. L. Gole, J. D. Stout, C. Burda, Y. Lou, X. Chen, The Journal of Physical Chemistry B **2004**, 108, 1230.

- [8] Y. Ma, X. Wang, Y. Jia, X. Chen, H. Han, C. Li, *Chemical Reviews* **2014**, 114, 9987.
- [9] M. Ni, M. K. H. Leung, D. Y. C. Leung, K. Sumathy, *Renewable and Sustainable Energy Reviews* **2007**, 11, 401.
- [10] S. N. Habisreutinger, L. Schmidt-Mende, J. K. Stolarczyk, *Angewandte Chemie International Edition* **2013**, 52, 7372.
- [11] A. T. Garcia-Esparza, K. Takanabe, *Journal of Materials Chemistry A* **2016**, 4, 2894.
- [12] J. H. Montoya, L. C. Seitz, P. Chakthranont, A. Vojvodic, T. F. Jaramillo, J. K. Norskov, *Nature Mater.* **2017**, 16, 70.
- [13] R. Abe, K. Sayama, H. Sugihara, *The Journal of Physical Chemistry B* **2005**, 109, 16052.
- [14] A. Kudo, Y. Miseki, *Chemical Society Reviews* **2009**, 38, 253.
- [15] N. S. Lewis, *Science* **2007**, 315, 798.
- [16] H. Zhou, R. Yan, D. Zhang, T. Fan, *Chemistry – A European Journal* **2016**, 22, 9870.
- [17] K. Teramura, S. Iguchi, Y. Mizuno, T. Shishido, T. Tanaka, *Angewandte Chemie International Edition* **2012**, 51, 8008.
- [18] N. Ahmed, Y. Shibata, T. Taniguchi, Y. Izumi, *Journal of Catalysis* **2011**, 279, 123.
- [19] Y. Zhao, X. Jia, G. I. N. Waterhouse, L.-Z. Wu, C.-H. Tung, D. O'Hare, T. Zhang, *Advanced Energy Materials* **2016**, 6, 1501974.
- [20] Y. Zhao, G. Chen, T. Bian, C. Zhou, G. I. N. Waterhouse, L.-Z. Wu, C.-H. Tung, L. J. Smith, D. O'Hare, T. Zhang, *Advanced Materials* **2015**, 27, 7824.

- [21] K.-i. Katsumata, K. Sakai, K. Ikeda, G. Carja, N. Matsushita, K. Okada, *Materials Letters* **2013**, 107, 138.
- [22] J. Hong, W. Zhang, Y. Wang, T. Zhou, R. Xu, *ChemCatChem* **2014**, 6, 2315.
- [23] S. Liu, N. Zhang, Z.-R. Tang, Y.-J. Xu, *ACS Applied Materials & Interfaces* **2012**, 4, 6378.
- [24] S.-M. Xu, H. Yan, M. Wei, *The Journal of Physical Chemistry C* **2017**, 121, 2683.
- [25] S.-M. Xu, T. Pan, Y.-B. Dou, H. Yan, S.-T. Zhang, F.-Y. Ning, W.-Y. Shi, M. Wei, *The Journal of Physical Chemistry C* **2015**, 119, 18823.
- [26] Y. Surendranath, D. G. Nocera, in *Progress in Inorganic Chemistry*, John Wiley & Sons, Inc., **2011**, 505.
- [27] S. Kumar, M. A. Isaacs, R. Trofimovaite, L. Durndell, C. M. A. Parlett, R. E. Douthwaite, B. Coulson, M. C. R. Cockett, K. Wilson, A. F. Lee, *Applied Catalysis B: Environmental* **2017**, 209, 394.
- [28] Y. Dou, S. Zhang, T. Pan, S. Xu, A. Zhou, M. Pu, H. Yan, J. Han, M. Wei, D. G. Evans, X. Duan, *Advanced Functional Materials* **2015**, 25, 2243.
- [29] C. A. Antonyraj, P. Koilraj, S. Kannan, *Chemical Communications* **2010**, 46, 1902.
- [30] F. Song, X. Hu, *Nature Commun.* **2014**, 5, 4477.
- [31] K. S. W. Sing, D. H. Everett, R. A. W. Haul, L. Moscou, R. A. Pierotti, J. Rouquerol, T. Siemieniewska, in *Handbook of Heterogeneous Catalysis*, Wiley-VCH Verlag GmbH & Co. KGaA, **2008**, 3:3.3:3.3.1:1217.
- [32] X. Zheng, D. Yu, F.-Q. Xiong, M. Li, Z. Yang, J. Zhu, W.-H. Zhang, C. Li, *Chemical Communications* **2014**, 50, 4364.

- [33] J. Ding, Z. Huang, J. Zhu, S. Kou, X. Zhang, H. Yang, **2015**, 5, 17773.
- [34] Y.-C. Liu, J. A. Koza, J. A. Switzer, *Electrochimica Acta* **2014**, 140, 359.
- [35] Y. Y. Du, Q. Jin, J. T. Feng, N. Zhang, Y. F. He, D. Q. Li, *Catalysis Science & Technology* **2015**, 5, 3216.
- [36] P. Li, P.-P. Huang, F.-F. Wei, Y.-B. Sun, C.-Y. Cao, W.-G. Song, *Journal of Materials Chemistry A* **2014**, 2, 12739.
- [37] C. Dette, M. A. Pérez-Osorio, C. S. Kley, P. Punke, C. E. Patrick, P. Jacobson, F. Giustino, S. J. Jung, K. Kern, *Nano Letters* **2014**, 14, 6533.
- [38] G.-L. Tian, H.-B. He, J.-D. Shao, *Chinese Physics Letters* **2005**, 22, 1787.
- [39] H. Ünal, O. Gülsen, Ş. Ellialtıoğlu, E. Mete, *Physical Review B* **2014**, 89, 205127.
- [40] E. Baldini, L. Chiodo, A. Dominguez, M. Palummo, S. Moser, M. Yazdi-Rizi, G. Auböck, B. P. P. Mallett, H. Berger, A. Magrez, C. Bernhard, M. Grioni, A. Rubio, M. Chergui, *Nature Communications* **2017**, 8, 13.
- [41] J. M. Frost, K. L. M. Harriman, M. Murugesu, *Chemical Science* **2016**, 7, 2470.
- [42] Z. Liu, R. Ma, Y. Ebina, N. Iyi, K. Takada, T. Sasaki, *Langmuir* **2007**, 23, 861.
- [43] Y. Qiu, B. Lin, F. Jia, Y. Chen, B. Gao, P. Liu, *Materials Research Bulletin* **2015**, 72, 235.
- [44] D. O. Scanlon, C. W. Dunnill, J. Buckeridge, S. A. Shevlin, A. J. Logsdail, S. M. Woodley, C. R. A. Catlow, M. J. Powell, R. G. Palgrave, I. P. Parkin, G. W. Watson, T. W. Keal, P. Sherwood, A. Walsh, A. A. Sokol, *Nature Mater.* **2013**, 12, 798.

- [45] S. Kumar, S. T, B. Kumar, A. Baruah, V. Shanker, *The Journal of Physical Chemistry C* **2013**, 117, 26135.
- [46] K. Das, S. N. Sharma, M. Kumar, S. K. De, *The Journal of Physical Chemistry C* **2009**, 113, 14783.
- [47] K. Selvam, M. Swaminathan, *RSC Advances* **2012**, 2, 2848.
- [48] G. R. Dey, A. D. Belapurkar, K. Kishore, *Journal of Photochemistry and Photobiology A: Chemistry* **2004**, 163, 503.
- [49] Y. Nie, W.-N. Wang, Y. Jiang, J. Fortner, P. Biswas, *Catalysis Science & Technology* **2016**, 6, 6187.
- [50] W. Kim, G. Yuan, B. A. McClure, H. Frei, *Journal of the American Chemical Society* **2014**, 136, 11034.
- [51] S. Xie, Y. Wang, Q. Zhang, W. Deng, Y. Wang, *Chemical Communications* **2015**, 51, 3430.
- [52] P. Reñones, A. Moya, F. Fresno, L. Collado, J. J. Vilatela, V. A. de la Peña O'Shea, *Journal of CO<sub>2</sub> Utilization* **2016**, 15, 24.
- [53] C. Gao, Q. Meng, K. Zhao, H. Yin, D. Wang, J. Guo, S. Zhao, L. Chang, M. He, Q. Li, H. Zhao, X. Huang, Y. Gao, Z. Tang, *Advanced Materials* **2016**, 28, 6485.
- [54] Z. Q. He, D. Wang, H. Y. Fang, J. M. Chen, S. Song, *Nanoscale* **2014**, 6, 10540.
- [55] D. Wang, Y. Yu, Z. Zhang, H. Fang, J. Chen, Z. He, S. Song, *Environmental Science and Pollution Research* **2016**, 23, 18369.
- [56] R. Chong, B. Wang, C. Su, D. Li, L. Mao, Z. Chang, L. Zhang, *Journal of Materials Chemistry A* **2017**, 5, 8583.

- [57] J. Guo, C. Mao, R. Zhang, M. Shao, M. Wei, P. Feng, *Journal of Materials Chemistry A* **2017**, *5*, 11016.
- [58] Z. Zheng, B. Huang, X. Qin, X. Zhang, Y. Dai, *Chemistry – A European Journal* **2010**, *16*, 11266.
- [59] C. M. A. Parlett, M. A. Isaacs, S. K. Beaumont, L. M. Bingham, N. S. Hondon, K. Wilson, A. F. Lee, *Nature Mater.* **2016**, *15*, 178.

**Heterojunction nanocomposites** formed between visible and UV light absorbing Co-Al layered double hydroxide and anatase semiconductor nanostructures respectively are efficient photocatalysts for CO<sub>2</sub> reduction under solar irradiation without requiring sacrificial agents.

### Photocatalytic CO<sub>2</sub> reduction

S. Kumar, L. J. Durndell, J. C Manayil, M. A. Isaacs, C. M. A. Parlett, S. Karthikeyan, R. E. Douthwaite, B. Coulson, K. Wilson, A. F. Lee\*

### Delaminated CoAl-layered double hydroxide@TiO<sub>2</sub> heterojunction nanocomposites for CO<sub>2</sub> photocatalytic reduction

